

# A Plasma Torus Around a Young Low-Mass Star

LUKE G. BOUMA<sup>1,2,\*</sup> AND MOIRA M. JARDINE<sup>3</sup>

<sup>1</sup>*Observatories of the Carnegie Institution for Science, Pasadena, CA 91101, USA*

<sup>2</sup>*Department of Astronomy, California Institute of Technology, Pasadena, CA 91125, USA*

<sup>3</sup>*School of Physics and Astronomy, University of St Andrews, North Haugh, St Andrews, Fife, Scotland KY16 YSS, UK*

(Received 23 April 2025; Revised 29 May 2025; Accepted –)

## ABSTRACT

A small fraction of red dwarfs younger than  $\sim 100$  million years show structured, periodic optical light curves suggestive of transiting opaque material that corotates with the star. However, the composition, origin, and even the existence of this material are uncertain. The main alternative hypothesis is that these complex periodic variables (CPVs) are explained by complex distributions of bright or dark regions on the stellar surfaces. Here, we present time-series spectroscopy and photometry of a rapidly-rotating ( $P=3.9$  hr) CPV, TIC 141146667. The spectra show sinusoidal time-varying H $\alpha$  emission at twice to four times the star’s equatorial velocity, providing direct evidence for cool ( $\lesssim 10^4$  K) plasma clumps trapped in corotation around a CPV. These data support the idea that young, rapidly-rotating M dwarfs can sustain warped tori of cool plasma, similar to other rapidly-rotating magnetic stars. Outstanding questions include whether dust clumps in these plasma tori explain CPV light curves, and whether the tori originate from the star or are fed by external sources. Rough estimates suggest  $\gtrsim 10\%$  of M dwarfs host similar structures during their early lives.

**Keywords:** Circumstellar matter (241), Stellar magnetic fields (1610), Stellar rotation (1629) Periodic variable stars (1213), Weak-line T Tauri stars (1795)

## 1. INTRODUCTION

Stars with masses below about half that of the Sun, M dwarfs, are the only type of star to offer near-term prospects for detecting the atmospheres of rocky exoplanets with surface water. Community investment with JWST is proceeding accordingly (Redfield et al. 2024; TRAPPIST-1 JWST Community Initiative et al. 2024). The question of how M dwarfs influence their planets—especially the retention of their atmospheres—has correspondingly grown in importance. Previous work has established that most M dwarfs host close-in planets (Dressing & Charbonneau 2015) that on average are subject to long disk lifetimes (Ribas et al. 2015), intense UV radiation (France et al. 2016), and frequent stellar flares (Feinstein et al. 2020). However, despite extensive work in these areas, the plasma and magnetospheric environments that bathe young, close-in exoplanets remain challenging to quantify. Understanding these environments is crucial because they directly impact atmospheric retention and, ultimately, habitability.

One example of our current ignorance is the complex periodic variables. While Figure 1 highlights the main object of interest in this article, over one hundred analogous systems have now been found by K2 and TESS (Rebull et al.

2016; Stauffer et al. 2017; Rebull et al. 2018; Zhan et al. 2019; Rebull et al. 2020; Stauffer et al. 2021; Popinchalk et al. 2023; Bouma et al. 2024). These CPVs are phenomenologically identified based on their structured, periodic optical light curves; most are M dwarfs with rotation periods shorter than two days. Within current sensitivity limits, none host disks (Stauffer et al. 2017; Bouma et al. 2024). However,  $\approx 3\%$  of stars a few million years old show this complex behavior, an observed fraction which decreases to  $\approx 0.3\%$  by  $\approx 110$  Myr (Rebull et al. 2020). CPVs can and have been confused for transiting exoplanets (van Eyken et al. 2012; Johns-Krull et al. 2016; Bouma et al. 2020).

The two leading hypotheses for explaining CPVs are either that transiting clumps of circumstellar material corotate with the star (Stauffer et al. 2017), or that these stars represent an extreme in naturally-occurring distributions of starspots or faculae (Koen 2021). The main argument against a starspot-only explanation invokes the timescales and amplitudes of the sharpest photometric features. However, no independent evidence has yet been acquired for the presence of any circumstellar material. If such material exists, then the geometric correction from the transit probability would imply an intrinsic occurrence rate at least a few times larger than the observed rate, suggesting that these clumps could exist around  $\gtrsim 10\%$  of M dwarfs during their early lives.

The dearth of evidence for circumstellar material around CPVs is surprising given that separate studies of young stars have, for decades, reported that stellar coronae contain both

Corresponding author: Luke G. Bouma

\* Carnegie Fellow; 51 Pegasi b Fellow



**Figure 1 (Movie).** TIC 141146667 is a complex periodic variable (CPV). The online movie, [available here](#), covers a baseline of 5,784 cycles irregularly sampled over three years. The TESS light curve is phased to the 3.930 hour period in groups of three cycles per frame. This is the period both of stellar rotation, and (we hypothesize) of corotating clumps of circumstellar material. Raw data acquired at two minute cadence are in gray; black averages to 100 points per cycle. The sharp photometric features persist for tens to thousands of rotational cycles.

hot ( $\gtrsim 10^6$  K) and cool ( $\lesssim 10^4$  K) plasma. In particular, time-series spectroscopy of stars with a wide range of masses has shown periodic high-velocity absorption and emission in Balmer lines such as  $H\alpha$ , interpreted as long-lived, corotating clumps of cool plasma (Collier Cameron & Robinson 1989; Collier Cameron & Woods 1992; Barnes et al. 2000; Donati et al. 2000; Dunstone et al. 2006; Skelly et al. 2008; Leitzinger et al. 2016; Cang et al. 2021). Such clumps are thought to be forced into corotation by the star’s magnetic field, and the exact geometry of where the plasma can accumulate is dictated by the field’s topology (Wagh & Jardine 2022). For instance, a magnetic dipole field tilted with respect to the stellar spin axis yields accumulations in a warped torus geometry (Townsend & Owocki 2005). To date, none of these spectroscopic variables have shown any photometric anomalies (Bouma et al. 2024), leaving open the issue of whether they are related to CPVs.

In this study, we present the first spectroscopic detection of corotating clumps of cool plasma around a CPV, TIC 141146667. Section 2 describes our observations; Section 3 presents the results; Section 4 discusses their interpretation and highlights future directions.

**Table 1.** Selected properties of TIC 141146667.

Parameter	Description	Value	Source
$T_{\text{eff}}$	Effective Temperature (K)	$2972 \pm 40$	1
$R_*$	Stellar radius ( $R_\odot$ )	$0.42 \pm 0.02$	1
Age	Stellar age range (Myr)	35-150	2
$M_*$	Stellar mass ( $M_\odot$ )	$0.22 \pm 0.02$	3
$\gamma$	Systemic radial velocity ( $\text{km s}^{-1}$ )	$0.61 \pm 1.47$	4
SpT	Spectral Type	M5.5Ve	4
$P_{\text{rot}}$	Photometric rotation period (hr)	$3.930 \pm 0.001$	5
$v_{\text{eq}}$	Equatorial velocity	$130 \pm 4$	6
	( $2\pi R_*/P_{\text{rot}}$ ) ( $\text{km s}^{-1}$ )		
$v_{\text{eq}} \sin i_*$	Projected rotational velocity	$138 \pm 8$	4
	( $\text{km s}^{-1}$ )		
$v_{\text{crit}}$	Critical velocity	$316 \pm 16$	6
	( $GM_*/R_*^{1/2}$ ) ( $\text{km s}^{-1}$ )		
$i_*$	Stellar inclination	$>63$	4
	$2\sigma$ lower limit (deg)		
$d$	Distance (pc)	$57.54 \pm 0.09$	7
$R_c$	Keplerian corotation radius ( $R_*$ )	$1.82 \pm 0.10$	6
$a_0$	Mean inner clump (0) orbital radius ( $R_*$ )	$2.07 \pm 0.04$	4
$a_1$	Mean inner clump (1) orbital radius ( $R_*$ )	$2.88 \pm 0.10$	4
$a_2$	Mean outer clump orbital radius ( $R_*$ )	$3.88 \pm 0.25$	4
$\langle \text{EW}_{H\alpha} \rangle$	Time-averaged $H\alpha$ line core equivalent width ( $\text{\AA}$ )	$7.2 \pm 0.2$	4

NOTE—Provenances are: 1: SED fit (Bouma et al. 2024). 2: Gaia DR3 photometry shows the star is on the pre-main sequence, while the spectrum lacks lithium (Appendix A). 3: PARSEC v1.2S (Chen et al. 2014). 4: Keck/HIRES (Appendix B). 5: TESS light curve. 6: Derived quantity. 7: Gaia DR3 geometric (Gaia Collaboration et al. 2023).

## 2. OBSERVATIONS

We identified TIC 141146667 in previous work (Bouma et al. 2024) by searching TESS two-minute data from 2018-2022 for highly structured, periodic light curves (Ricker et al. 2015). We chose the star for spectroscopy because its brightness and rapid rotation enabled an efficient search for variability in its line profiles. As an apparently single pre-main sequence M dwarf, its properties are typical for the CPV population (see Table 1 and Appendix A).

We observed TIC 141146667 ( $V=16.2$ ) for five hours on 17 February 2024 using the High Resolution Echelle Spectrometer (HIRES; Vogt et al. 1994) on the 10 m Keck I telescope. The observations spanned the second half of the night, from 10:47 to 16:13 (UT). We opted for a fixed 15 minute cadence, and used the C2 decker ( $0''.86 \times 14''.0$ ) in the red configuration, yielding a resolution  $R \approx 45,000$  ( $\delta v \approx 6.7 \text{ km s}^{-1}$ ).

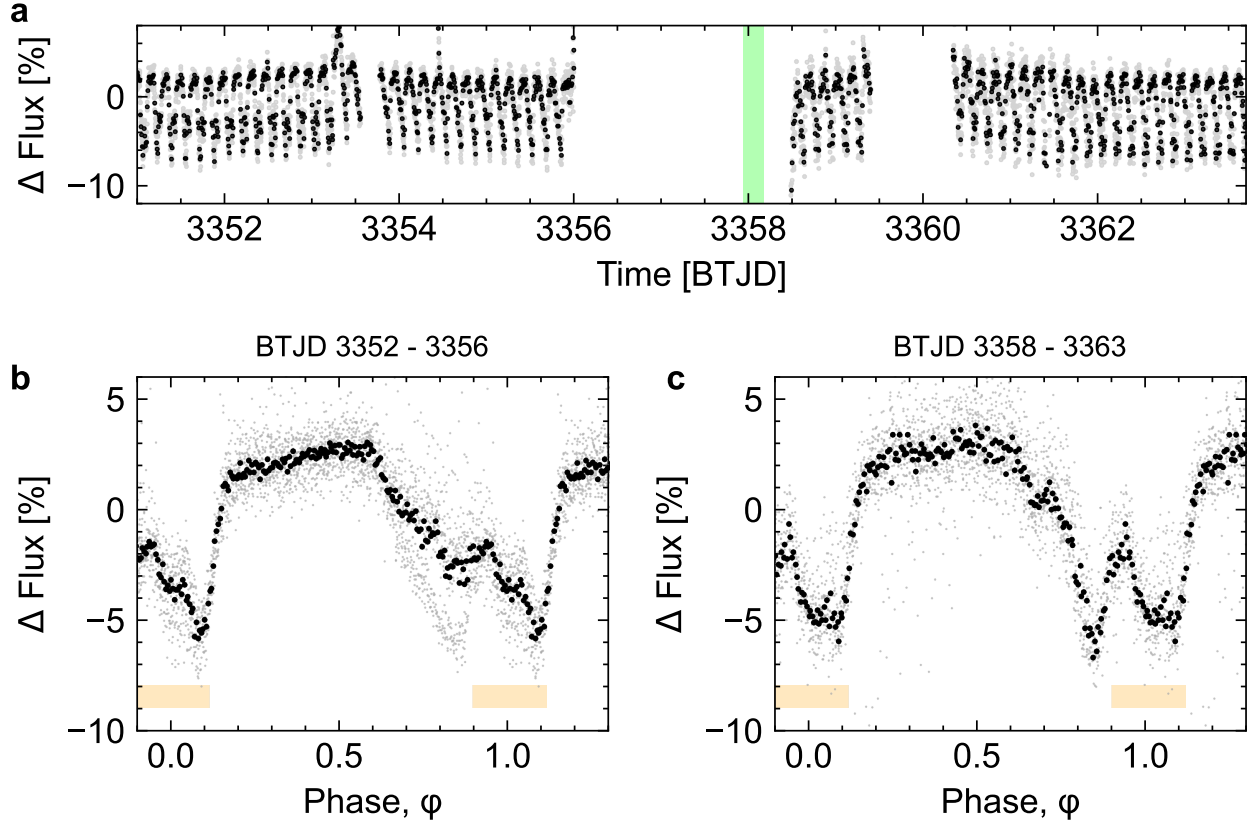


**Figure 2. Photometric evolution of TIC 141146667 during the Keck/HIRES observation (green bar).** **a**, TESS simple aperture photometry. Data gaps were caused by stray light from the Earth (BTJD 3356-3358.5) and Moon (BTJD 3359.5-3360.5). Raw two minute data are in gray; black time-averages to ten minute sampling. **b-c**, Folded TESS light curve before and after spectroscopy. Black now phase-averages to 100 points per 3.93 hour cycle. During BTJD 3352-3356, a state switch occurred near BTJD 3353, and the dip at  $\phi \approx 0.8$  became less pronounced. While the dip spanning  $\phi = 0.6$ -1.1 was present both before and after the HIRES sequence, its photometric shape evolved during the data gap. The orange bar denotes times of spectroscopic transits for the inner two  $H\alpha$  clumps observed with HIRES (see Figure 3).

Strong winds contributed to  $1''$ - $1.5''$  seeing, but conditions were otherwise favorable. We reduced the echelleogram using the standard techniques of the California Planet Survey (Howard et al. 2010).

TESS observed TIC 141146667 ( $T=13.3$ ) for six non-contiguous months spanning 2019-2024. TESS acquired these observations at two-minute cadence during Sectors 41, 48, and 75. The 30-minute data during Sectors 14, 15, and 21 smeared sharp features over the star's 3.93 hour period (see Günther et al. 2022). The movie in Figure 1 shows the two-minute data: like other CPVs, TIC 141146667 maintains a fixed period over timescales of years while its detailed photometric morphology evolves. The nearest known star, TIC 141146666 ( $T=14.5$ ), is  $25''$  from TIC 141146667 and is photometrically quiet; crowding is not a concern.

We observed with Keck during Sector 75 in an attempt to obtain simultaneous observations. Figure 2 shows the result; Earth passed within  $25^\circ$  of the TESS camera's boresight from BTJD 3356.0-3358.5, which caused a data gap that ended twelve hours after our Keck/HIRES observations (green bar). From BTJD 3359.4-3362.0, the Moon then passed within  $25^\circ$  of the camera's boresight. Based on the level of scattered

light in the optimal aperture (Jenkins et al. 2016), we manually masked out data in the TESS light curve from 3359.4-3360.1; the remainder of the data during the lunar approach were usable. Small gaps from BTJD 3353.6-3353.8 and 3360.1-3360.3 were caused by data downlinks at the spacecraft's perigee and apogee.

While the data gap is unfortunate, Figure 2 shows that both before and after the HIRES data were acquired, a large flux decrement spanned roughly half of each cycle. From BTJD 3352-3356, this dip had two sharp local minima; the minimum at  $\phi \approx 0.8$  became less pronounced following the flare at BTJD 3353, yielding a dip more closely resembling an asymmetric "V" than a "W". Similar CPV state changes have been previously seen (Stauffer et al. 2017; Bouma et al. 2024). The photometric shape therefore evolved during the twelve cycles spanning the 3356-3358 gap, since the average shape from 3358-3363 more closely resembles the initial "W". Nonetheless, the global photometric morphology—a small brightening over 45% of the period, followed by a complex flux dip spanning 55% of the period—is similar before and after the data gap.

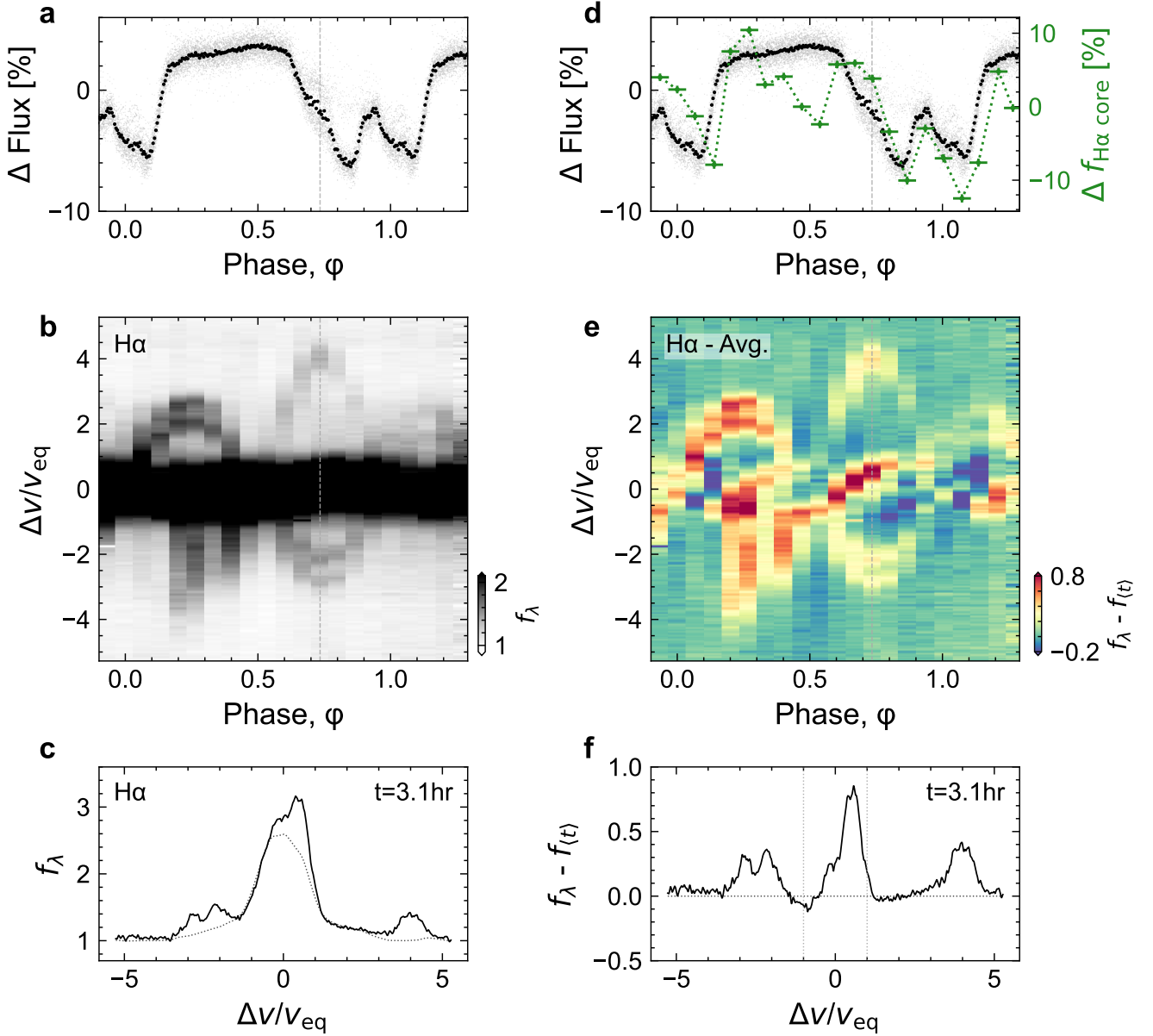


**Figure 3 (Movie).** Emission from plasma clumps orbiting TIC 141146667. The online movie, [available here](#), shows the spectral evolution over five hours. **a**, TESS light curve from 5 February 2024 to 26 February 2024 folded on the 3.93 hour period. Black points are phase-averaged; gray are the raw data. **b**, Keck/HIRES H $\alpha$  spectra from 17 February 2024. The continuum is set to unity, and the darkest color is at twice the continuum to accentuate emission outside the line core ( $|v/v_{\text{eq}}| > 1$ , for the equatorial velocity  $v_{\text{eq}}=130 \text{ km s}^{-1}$ ). While emission within the line core comes from the star’s chromosphere, the sinusoidal emission features are most readily described by a warped plasma torus. **c**, Individual epochs of Panel b, visible in the online movie. The dotted line shows the time-averaged spectrum,  $f_{(t)}$ . **d**, As in Panel a, but overplotting the median-normalized H $\alpha$  light curve at  $|v/v_{\text{eq}}| < 1$ . **e**, As in Panel b, after subtracting  $f_{(t)}$ . The line core shows H $\alpha$  excesses and decrements advancing from the blue to red wings. The asymmetric color stretch mirrors the dynamic range of the data. **f**, Individual epochs of Panel e, visible in the online movie. A separate version with best-fit sinusoids overplotted is also [available](#).

### 3. RESULTS

Figure 3 shows the TESS and HIRES data from February 2024. The spectra (Panels b,c) show emission in H $\alpha$  beyond the star’s equatorial velocity,  $v_{\text{eq}}$ , of  $130 \text{ km s}^{-1}$ . There are at least two distinct emission components,  $180^\circ$  apart in phase. The inner component at lower velocities has clearer

sinusoidal behaviour in time and is double-peaked, with peak semi-amplitudes of  $2.07 v_{\text{eq}}$  and  $2.88 v_{\text{eq}}$  (see Appendix B). There is significant non-periodic variability in the emissivity of this double-peaked component: the flux excess begins with an amplitude 70% above the continuum, and diminishes to 10% by sunrise. The higher-velocity component  $180^\circ$  op-



posite in phase is detected only from  $\phi=0.2$ -1.0. From  $\phi=0.2$ -0.5, this outer component appears connected to the star in velocity space. While its peak semi-amplitude of  $3.88 v_{\text{eq}}$  is achieved at both  $\phi=0.25$  and  $\phi=0.75$ , its amplitude similarly decreases from a 60% excess to a 10% excess over the observation sequence. In Appendix B, we measured the period for all three emission components to be consistent with the photometric 3.930 hour period, to within two minutes for the inner component.

These sinusoidal emission features require circumstellar clumps of partially-ionized hydrogen to corotate with the star. Based on the observed sinusoidal periods and velocities, this material is not moving on a Keplerian orbit; it is magnetically forced to co-rotate with the star. The velocity semi-amplitude of the sinusoids gives the mean distance of each clump from the stellar rotation axis:  $2.07 R_*$  and  $2.88 R_*$  for the inner clumps, and  $3.88 R_*$  for the outer clump. These clumps transit in front of the star when passing from negative to positive velocity. The transits of the two inner clumps last  $\approx 22\%$  of each cycle, from  $\phi=-0.1$  to  $\phi=+0.12$ . This spectroscopic transit coincides with the latter half of the complex eclipse feature in the TESS data (see Figure 2 and Panels a and b of Figure 3).

The  $H\alpha$  line core, visible in Panels e and f of Figure 3, is more complex. At  $|\Delta v/v_{\text{eq}}| < 1$ , most observed  $H\alpha$  photons come from the star's chromosphere; variability in the stellar emission line can be caused by circumstellar material, bright regions, or dark regions crossing the star's surface. Figure 3e suggests that all three effects occur in TIC 141146667. For instance, from  $\phi=0$ -0.3, double-peaked emission is visible both on and off-limb; this feature is circumstellar in origin. However, the emission feature that crosses the star from  $\phi=0.4$ -0.9 is brighter than the circumstellar clumps, and its slow speed instead suggests it is associated with a bright region on the star's surface. Similarly, from  $\phi=0.6$ -1.15 a 20% deep absorption feature slowly crosses the  $H\alpha$  line profile. This feature could be either a chromospherically dark region (e.g. a spot group), or an azimuthally extended component of the circumstellar material. The origin of the other bright and dark streaks passing across the line core in Figure 3e is similarly ambiguous.

Figure 3d shows a final exercise to quantify the behavior of the line core, by summing the  $H\alpha$  flux at  $|\Delta v/v_{\text{eq}}| < 1$ . This panel shows that changes in the line core flux ( $f_{H\alpha \text{ core}}$ ) correlate with the broadband variability throughout most of the light curve, except near  $\phi \approx 0.5$ , corresponding to the transit of the  $3.9 R_*$  clump and the occultation of the lower-velocity clump. Spectroscopic transits may therefore not always be associated with photometric transits.

## 4. DISCUSSION

### 4.1. Physical Properties of the Emitting Region

Our Keck/HIRES observations are the first reported time-series spectra of a CPV, and they demonstrate that corotating circumstellar plasma clumps exist around at least one such star. More specifically, the spectra require plasma with a significant population of hydrogen in the  $n=3$  excited state, with

minimal evidence for higher-order excitations. Most of this  $H\alpha$  emission originates in “clumps” with size comparable to the star; radial “spokes” or azimuthally extended “arcs” for the emitting material are ruled out by the  $\approx 30 \text{ km s}^{-1}$   $H\alpha$  velocity dispersion (see Appendix B). The  $H\alpha$  line luminosity suggests characteristic number densities and masses for the gaseous component of these clumps of  $n_{\text{H}} \sim 10^{11} \text{ cm}^{-3}$  and  $M_{\text{gas}} \sim 10^{17} \text{ g}$  (see Appendix C). Dust is independently constrained to have a total mass  $M_{\text{dust}} < 10^{17} \text{ g}$  based on the lack of a WISE infrared excess; if one assumes that the opacity in the TESS flux dips comes from dust, a lower limit  $M_{\text{dust}} > 10^{15} \text{ g}$  follows (see Appendix D).

### 4.2. Clumps Within Warped Plasma Tori

While the  $H\alpha$  emission mostly comes from clumps, the broadband flux dip in Figure 3 spans roughly half of each cycle. In CPVs more generally, individual flux dips last 5-50% of each cycle, and there are often multiple dips per cycle (Bouma et al. 2024). This implies that azimuthally-distributed material may be the norm for CPVs; a warped torus may be a more accurate picture than a clump.

Townsend & Owocki (2005) outlined the physics of how rapidly-rotating stars with strong magnetic fields can support plasma tori (see also Nakajima 1985; Ferreira 2000; Petit et al. 2013; Daley-Yates & Jardine 2024). When the magnetospheric radii  $R_{\text{m}}$  of such stars exceeds their Keplerian corotation radii  $R_{\text{c}}$ , the effective potential (gravitational plus centrifugal) experienced by plasma along any given field line has a local minimum outside  $R_{\text{c}}$ , which enables charged material to accumulate in a torus. Warps can occur when there is misalignment between the spin and magnetic axes. In general, the regions in these centrifugally-supported magnetospheres with the densest plasma accumulations need neither transit nor be opaque in broadband optical light.

In a follow-up study, Townsend (2008) made synthetic light curves, assuming that the optical depth scaled linearly with plasma density. They found that W-shaped eclipses, similar to those seen for TIC 141146667, can occur when the spin and magnetic axes are moderately ( $15$ - $45^\circ$ ) misaligned. The movies associated with their work are available online<sup>§</sup>; for a  $\omega/\omega_{\text{c}} \approx 0.5$  edge-on system like TIC 141146667, the photometric eclipses have the correct shape, and the  $H\alpha$  emission similarly exhibits double-peaked behavior. The plasma clumps in this model are  $180^\circ$  apart because the deepest local minima in the effective potential exist along the line of intersection between the rotational and magnetic planes (see Equation 22 of Townsend & Owocki 2005).

To summarize, the evidence for warped plasma tori in TIC 141146667 and CPVs more broadly is that Figure 3 shows two plasma clumps separated by  $180^\circ$  in phase; the warped-torus model predicts both “W” shaped photometric eclipses and double-peaked  $H\alpha$  morphology at quadrature; and CPV dips last 5-50% of each cycle, indicating an az-

<sup>§</sup> [http://user.astro.wisc.edu/~townsend/static.php?ref=rrm-movies#Download\\_Bundles](http://user.astro.wisc.edu/~townsend/static.php?ref=rrm-movies#Download_Bundles) last accessed 28 May 2025.

imutally extended distribution of material. However, two challenges remain. First, the model predicts *two* W-shaped eclipses per cycle. Second, it predicts that the antipodal clumps should lie at equal distances from the star. Different clump opacities or non-dipolar magnetic fields might resolve these discrepancies. Overall, the evidence suggests a warped torus is a good first approximation, but one that will need refinement in future work.

### 4.3. Origin of CPV Photometric Variability and Astrophysical Analogs

Microphysically, it is not obvious whether hydrogen alone can produce the chromatic broadband flux variations seen in CPVs. The alternative is that charged dust could provide most of the opacity (Sanderson et al. 2023). For TIC 141146667, Figures 2 and 3 show that the transits of the inner H $\alpha$  clump only partially overlap the complex photometric modulation. This implies that some of the complex photometric dips must involve additional opacity sources or spatially distinct structures.

Independent of this opacity question, our observations show that corotating clumps of cool plasma exist around a CPV. While starspots do contribute smooth signals to CPV photometric variability, the existence of these clumps would not be predicted by a “starspot-only” scenario (Koen 2021). Scenarios in which the circumstellar material is made only of dust are similarly ruled out.

The circumstellar material – either pure plasma or dusty plasma – could originate either from the star or from an external source. Plausible external sources include an undetected old disk, comets, or a close-in exoplanet. This latter scenario would make CPVs extrasolar analogs of the Jupiter-Io torus (e.g. Bagenal & Sullivan 1981, Kislyakova et al. 2018), although with a very different composition.

The other CPV analog is the  $\sigma$  Ori E variables, a rare subset of B stars with radiatively-driven winds that accumulate into warped plasma tori (Townsend & Owocki 2005). These tori tend to have dense antipodal accumulations of plasma sculpted by tilted-dipole magnetic fields; these clumps produce broadband optical variability through bound-free scattering (Townsend & Owocki 2005) and Thomson scattering (Berry et al. 2022). For  $\sigma$  Ori E and most of its analogs, the result is simple light curves that resemble eclipsing binaries, and time-dynamic H $\alpha$  spectra similar to Figure 3. The two known exceptions, HD 37776 and HD 64740, have spectropolarimetric magnetic field maps indicating strong contributions from higher-order magnetic moments (Kochukhov et al. 2011; Shultz et al. 2018) and complex light curves resembling CPVs (Mikulášek et al. 2020; Bouma et al. 2024). This suggests that the photometric complexity of CPVs may be related to magnetic fields with highly multipolar contributions. While this suggestion is consistent with the wide range of axisymmetric and non-axisymmetric topologies seen in mid- and late-M dwarfs (e.g. Donati et al. 2006; Kochukhov & Lavail 2017; Shulyak et al. 2019; Bellotti et al. 2024), future work is needed to verify whether CPVs indeed select for complex, non-axisymmetric fields.

### 4.4. Connection to Previous Work

Spectra of magnetically-active, rapidly rotating stars with a wide range of masses have been previously observed to exhibit sinusoidal time-varying Balmer emission (Donati et al. 2000; Townsend et al. 2005; Dunstone et al. 2006; Skelly et al. 2008), similar to Figure 3. No such stars were previously known to show complex light curves (Bouma et al. 2024). One interpretation for the spectroscopic variability of these stars, and that of the analogous transient H $\alpha$  absorption features (Collier Cameron & Robinson 1989; Collier Cameron & Woods 1992; Cang et al. 2020), comes from an analogy to quiescent solar prominences, cool condensations of plasma in the solar corona that can last days to weeks (Vial & Engvold 2015). In the case of the Sun, these condensations fall back to the photosphere because gravity is stronger than any magnetic tension or centrifugal force capable of sustaining them. However, it has been understood at least since work by Donati et al. (2000) that these “prominence systems” can be longitudinally extended, forming a trapped ring of plasma. While the issue of why these previously known spectroscopic variables do not show complex photometric variability remains open, plausible explanations include that they are not in the required transiting geometry, or that they lack the necessary source of opacity. What we have in the case of TIC 141146667 is a system that finally exhibits both sets of phenomena.

### 4.5. Future Work: Composition, Origin, Modeling

Pressing issues include determining the composition and origin of the circumstellar material, understanding the exact role of the stellar magnetic field, and exploring the implied space weather experienced by the close-in rocky exoplanets that, statistically (Dressing & Charbonneau 2015), are likely to be present in many CPV systems.

The material’s composition – either pure plasma or dusty plasma – can be clarified by time-series infrared spectrophotometry. While observations of CPVs in the optical suggest chromaticity consistent with dust (Tanimoto et al. 2020; Günther et al. 2022; Koen 2023), electron scattering in a plasma transiting over a spotted star might also produce chromatic features (Rackham et al. 2018). This degeneracy is alleviated in the infrared, where the composition and size distribution of any dust that is present could be determined by measuring the extinction curve for a sample of CPVs from 1-20  $\mu$ m. Composition and size distributions similar to debris from rocky bodies seen around white dwarfs (Reach et al. 2009) would suggest an extrinsic origin channel. Compositions and sizes similar to the interstellar medium would suggest that dust can condense out from M dwarf winds, similar to processes that occur around evolved stars (Marigo et al. 2008).

Future models could take a range of steps to clarify the origin of CPVs. A first step for magnetohydrodynamic models that can currently explain the H $\alpha$  features (e.g. Waugh & Jardine 2022) would be to incorporate an opacity source that can reproduce the photometric dips. This effort will also require exploring what stellar magnetic field topologies reproduce the observed light curve shapes. While previous models

in the rigid-field approximation have explored both dipolar (Townsend 2008) and multipolar fields (Krtićka et al. 2022), dynamo simulations of fully-convective M dwarfs have suggested that global-scale mean fields might be confined to a single hemisphere (Brown et al. 2020); such fields would yield accumulation surfaces different from those that have been explored. One related challenge is that CPVs currently suffer a dearth of stellar surface field measurements, unlike benchmark systems such as AB Dor and V374 Peg (Jardine et al. 2002; Vidotto et al. 2011). This might be alleviated by future spectropolarimetry, or by radio observations sensitive to the magnetic field structure around the star (Callingham et al. 2021; Kaur et al. 2024). Finally, the question of what microphysical process yields the opaque material also merits future theoretical attention. While recent advances can produce the catastrophic cooling that leads to dense, cool clumps embedded in a hot corona (Daley-Yates et al. 2023; Daley-Yates & Jardine 2024), a self-consistent treatment of radiation propagating through such clumps has yet to be performed. Whether dust grains can form in these plasma clumps similarly deserves attention.

It is currently unclear what, if any, relationship CPVs have to the close-in rocky exoplanets that exist around most M dwarfs (Dressing & Charbonneau 2015). However, a few percent of young M dwarfs show the CPV phenomenon (Rebull et al. 2020), and our data show that some of the flux dips occur when clumps of circumstellar material transit the star. The geometric correction implies that an appreciable minority ( $\gtrsim 10\%$ ) of young M dwarfs—the rapidly rotating ones with centrifugal magnetospheres—host circumstellar environments similar to the CPVs. Future studies that combine spectroscopic, polarimetric, and multi-wavelength observations, along with magnetohydrodynamic modeling, will be key to understanding the complex environments of these young stars.

## ACKNOWLEDGEMENTS

We thank B. Tofflemire, A. Weinberger, and L. Hillenbrand for conversations that significantly informed this work;

J. Spake, J. Winn, J.-F. Donati, and R. Townsend for feedback on the manuscript; and A. Howard and H. Isaacson for their assistance reducing the HIRES spectra.

LGB acknowledges support from the Carnegie Fellowship and the Heising-Simons 51 Pegasi b Fellowship. MMJ acknowledges support from STFC consolidated grant number ST/R000824/1.

The analyses in this article used data from TESS. The 2-minute cadence observations from Sectors 41 & 48 were from TESS DDT039 (PI: M. Kunimoto) and the observations from Sector 75 were from TESS G06030 (PI: L. Bouma). The TESS data can be accessed through MAST via DOI 10.17909/t9-nmc8-f686. Funding for the TESS mission is provided by NASA’s Science Mission directorate. TESS is a product of millions of hours of work by thousands of people, and we thank the TESS team for their efforts to make the mission a continued success. The HIRES data were obtained at the Keck Observatory, which exists through a similar scale of community effort. We recognize the importance that the summit of Maunakea has always had within the indigenous Hawaiian community, and we are grateful for the opportunity to conduct observations from this mountain.

**Contributions:** LGB led the inception, design, execution, and interpretation of the project. MMJ contributed to the interpretation.

**Facilities:** Gaia (Gaia Collaboration et al. 2023), TESS (Ricker et al. 2015), Keck:I (HIRES) (Vogt et al. 1994), 2MASS (Skrutskie et al. 2006), SDSS (York et al. 2000).

**Software:** astroariadne (Vines & Jenkins 2022), astropy (Astropy Collaboration et al. 2013, 2018, 2022), chatgpt (Open-AI 2025), dustmaps (Green 2018), matplotlib (Hunter et al. 2007), numpy (Van Der Walt et al. 2011), numpyro (Phan et al. 2019), scipy (Virtanen et al. 2020).

## APPENDIX

### A. STELLAR PARAMETERS

**Radial Velocity**—We measured the radial velocities of TIC 141146667 (Gaia DR3 860453786736413568) from our HIRES spectra using a custom pipeline. Our method was based on template-matching against synthetic PHOENIX spectra (Husser et al. 2013), and was calibrated against the standard stars described by Chubak et al. (2012). We used velocity standards spanning G2-M4, irrespective of rotation rate. We included velocity corrections due to Earth’s motion around the solar system barycenter and due to Earth’s daily rotation about its axis, calculated using `barycorrpy` (Kanodia & Wright 2018). Our analysis code reproduced the systemic velocities of known velocity standards (Chubak et al. 2012) with an RMS of  $0.66 \text{ km s}^{-1}$ .

For TIC 141146667, we measured the radial velocities using regions near the K I (7700 Å) resonance line and three TiO bandheads (5160 Å, 5450 Å, and 5600 Å). We selected these regions because they provided the best matches between the synthetic and observed spectra. We averaged the redshift measurements over each order, and used the scatter of resulting velocity measurements between orders to assign the RV uncertainty at each epoch. The uncertainty-weighted mean systemic velocity over all epochs on 17 February 2024 was  $\gamma = 0.6 \pm 1.5 \text{ km s}^{-1}$ . The relative radial velocities about this mean are listed in Table 2.



**Figure 4. Spectral energy distribution** of broadband photometric magnitudes (filled cyan circles) plotted over the best-fit BT-Settl stellar atmosphere model (Allard et al. 2012) and the associated photometric predictions (empty purple diamonds). This plot was made from an adaptation of `astroARIADNE` (Vines & Jenkins 2022). The photometry extends from the Gaia DR3 blue passband to WISE W3; the W4 passband (22  $\mu\text{m}$ ) did not yield a confident detection. This fit yields the star’s temperature and size. The lack of excess infrared flux relative to the photospheric model sets an upper limit on emission from circumstellar dust.

*Viewing Orientation*—We fitted the rotational broadening of the K I (7700 Å) resonance line using the kernel suggested by Gray (2008); taking the mean and standard deviation of the resulting value over all epochs yielded  $v_{\text{eq}} \sin i = 138 \pm 8 \text{ km s}^{-1}$ , consistent with the visual line broadening  $\Delta\lambda \approx 3 \text{ Å}$ . The star’s equatorial velocity  $v_{\text{eq}}$  based on its apparent size and rotation period is  $130 \pm 4 \text{ km s}^{-1}$ . While these measurements are consistent with an edge-on viewing geometry, the formal constraint is rather weak, with  $i > 63^\circ$  at  $2\sigma$  (2.5<sup>th</sup> percentile of the inclination posterior).

*No Evidence For Binarity*—Any periodicity in the radial velocity time-series is ruled out at the rotation period for semi-amplitudes above  $2.85 \text{ km s}^{-1}$  (at  $3\sigma$  confidence). This sets an upper limit on the mass of any putative companion on a four hour orbit of  $m \sin i < 2.4 M_{\text{Jup}}$ . Regarding possible companions at wider separations, the Gaia DR3 renormalized unit weight error (RUWE) is 1.23, within the usual range for apparently single sources. There are no resolved companions in the Gaia DR3 point source catalog. Finally, we checked the TESS light curve for evidence of secondary photometric periods by subtracting the mean CPV signal over each sector and performing a phase-dispersion minimization analysis (Stellingwerf 1978; Bhatti et al. 2021). There were no secondary periods in the TESS data. Previous work (Bouma et al. 2024) has shown that  $\approx 30\%$  of CPVs show evidence for binarity from RUWE, and  $\approx 40\%$  of CPVs show evidence for binarity based on the presence of secondary photometric periods. This agrees with analyses showing that multi-periodic low-mass stars are usually unresolved binaries (Tokovinin & Briceño 2018). Overall, the CPV binary fraction seems consistent with that of field M dwarfs (Winters et al. 2019), pointing to a weak or non-existent connection between the CPV phenomenon and (wide) binarity. For TIC 141146667 specifically, we find no evidence for stellar multiplicity.

*Effective temperature, radius, mass, and spectral classification*—We adopted the star’s effective temperature and radius measured using the spectral energy distribution (SED) fitting procedure described by Bouma et al. (2024). To summarize, this approach used `astroARIADNE` (Vines & Jenkins 2022) to fit broadband magnitudes from Gaia DR2, APASS, 2MASS, SDSS, and WISE W1 and W2 with the BT-Settl stellar atmosphere models (Allard et al. 2012). Free parameters included the stellar effective temperature, radius, reddening, surface gravity, and metallicity. The resulting best-fit SED is shown in Figure 4. This method has the most constraining power for the star’s effective temperature ( $2972 \pm 40 \text{ K}$ ) and radius ( $0.42 \pm 0.02 R_{\odot}$ ). We measured the star’s spectral type to be M5.5Ve by visually comparing the HIRES spectra against the photometric standards tabulated by Bochanski et al. (2007). We measured the equivalent width of the H $\alpha$  line by fitting a range of models to the time-averaged line profile shown in Figure 3, selecting the model that minimized the Bayesian information criterion, and numerically integrating this best fit model. We found a sum of two Gaussians to be preferred; our quoted result,  $\text{EW}_{\text{H}\alpha} = 7.2 \pm 0.2 \text{ Å}$ , comes from numerically integrating within  $|\Delta v / v_{\text{eq}}| < 1$ . Integrating over the entire line profile, including the broad wings, would yield  $\text{EW}_{\text{H}\alpha} = 10.2 \pm 0.3 \text{ Å}$ . Either value would classify the star as a weak-lined T Tauri (Briceño et al. 2019).



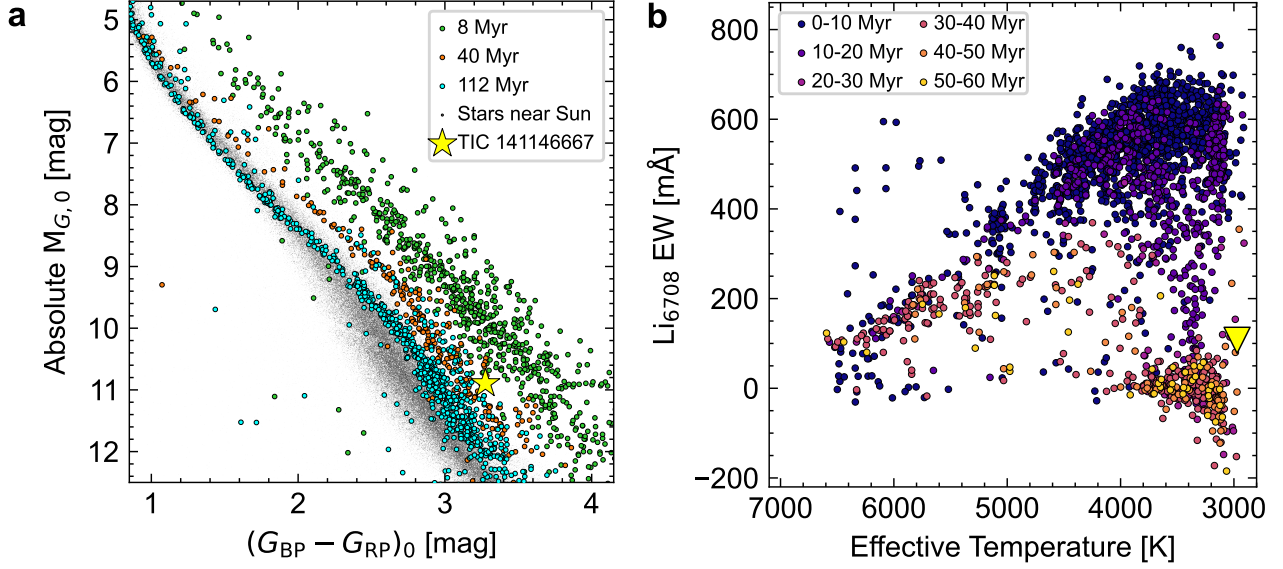


**Figure 5. TIC 141146667 age diagnostics.** **a**, Dereddened Gaia DR3 color vs. absolute magnitude for TIC 141146667, USco (8 Myr), IC 2602 (40 Myr), the Pleiades (112 Myr) and stars within 100 pc. The location of TIC 141146667 in this diagram suggests an age of 30–150 Myr. **b**, A dearth of photospheric lithium for TIC 141146667 (yellow triangle denotes  $2\sigma$  upper limit) yields a lower bound on the star’s age of  $\gtrsim 20$  Myr. Comparison stars are from the Gaia-ESO survey (Jeffries et al. 2023); rich clusters in these data include NGC 2264 (4.5 Myr),  $\lambda$  Ori (8.7 Myr),  $\gamma^2$  Vel (16.4 Myr), NGC 2547 (35.0 Myr), IC 2391 (42.0 Myr), and NGC 2451A (50.0 Myr). Measurement uncertainties are large below +50 mÅ; negative EW does not correspond to significant emission.

Given the effective temperature, stellar radius, and age range (35–150 Myr) derived below, we then estimated the stellar mass by interpolating against the PARSEC v1.2S isochrones (Chen et al. 2014), as in Bouma et al. (2024). This exercise yielded a mass of  $M_* = 0.20 \pm 0.01 M_\odot$  assuming an age of 35 Myr, or a mass of  $0.25 \pm 0.01 M_\odot$  assuming an age of 150 Myr. These masses imply Keplerian corotation radii  $R_{cr}/R_* = 1.75 \pm 0.07$  and  $R_{cr}/R_* = 1.89 \pm 0.07$ , respectively; this size scale is expected to set the inner boundary at which corotating material might accumulate (e.g. Townsend & Owocki 2005; Daley-Yates & Jardine 2024). Our final quoted  $M_*$  and  $R_{cr}$  values adopt the average of these extremes and a quadrature sum of their statistical uncertainties; a more precise age would be needed to resolve the systematic uncertainties in these parameters.

**Age: No Obvious Association Membership**—In Bouma et al. (2024) we previously found that over 90% of CPVs within 100 pc are associated with known young moving groups based on their positions and kinematics. TIC 141146667 is in the minority. We calculated the probability of TIC 141146667 being part of any nearby known group using BANYAN  $\Sigma$  v1.2 (Gagné et al. 2018). That particular model classifies it as a field star at  $>99.9\%$  confidence. We also searched the local vicinity of TIC 141146667 for neighbors with similar projected on-sky velocities using `comove` (Tofflemire et al. 2021). This yielded no strong candidates for co-moving stars with projected tangential velocities  $\Delta v_T < 5 \text{ km s}^{-1}$  that share its isochronal youth.

**Age: Isochrones**—The color and absolute magnitude of TIC 141146667 suggest that it is a pre-main sequence M dwarf, similar to all other known CPVs (Stauffer et al. 2017, 2021; Bouma et al. 2024). The star’s proximity ( $d=58$  pc) and high galactic latitude ( $b=+53^\circ$ ) yield negligible interstellar reddening along the line of sight (Green et al. 2019). Figure 5 shows the location of TIC 141146667 in the color–absolute magnitude diagram (CAMD) relative to young stellar populations including Upper Scorpius (USco), IC 2602, and the Pleiades. To make this diagram, we adopted the USco members in the  $\delta$  Sco and  $\sigma$  Sco sub-associations from Ratzenböck et al. (2023), and the IC 2602 and Pleiades members from Hunt & Reffert (2024). We assumed an average V-band extinction  $A_V = \{0.12, 0.11, 0.10\}$  mag for USco (Pecaut & Mamajek 2016), IC 2602 (Hunt & Reffert 2024), and the Pleiades (Hunt & Reffert 2024) respectively, and ages of 8 Myr (Ratzenböck et al. 2023), 40 Myr (Randich et al. 2018), and 112 Myr (Dahm 2015) for each respective cluster. We dereddened the photometry using the extinction coefficients  $k_X \equiv A_X/A_0$  tabulated in (Gaia Collaboration et al. 2018), assuming that  $A_0 = 3.1E(B-V)$ .

Figure 5 shows that TIC 141146667 falls between the USco and Pleiades sequences, and approximately overlaps IC 2602. However, the precision of the implied age is set by the intrinsic scatter of these calibration sequences; the most luminous stars in the Pleiades of the same color have a similar absolute magnitude as TIC 141146667. Previous work by Stauffer et al. (2021) has noted that in the Gaia passbands, CPVs tend to be photometrically redder and more luminous than single stars in any given cluster; they also found suggestive evidence for either hotspots or emission from dust based on analysis of Gaia and WISE photometry. The implication is that isochronal age dating of individual field CPVs suffers significant systematic uncertainty due

to factors including dark and bright spots, magnetic inflation, dust emission, and photometric binarity. Rather than adopting a particular model isochrone framework, we instead visually take the star’s location in the color–absolute magnitude diagram to suggest age bounds  $t_{\text{CAMD}} \sim 30\text{--}150$  Myr.

*Age: Lithium*—Lithium burning in the cores of low-mass stars has been studied for over sixty years (e.g. Hayashi & Nakano 1963; Bildsten et al. 1997). Wood et al. (2023) provided a recent overview; the brief summary is that sufficiently cool and young M dwarfs show the 6707.8 Å doublet in absorption,  $\gtrsim 10\%$  below their continua. However, unlike for Sun-like stars, the continuum for M dwarfs is challenging to define due to their molecular absorption. We therefore attempted a lithium measurement by constructing a wavelength-binned and Doppler-corrected TIC 141146667 spectrum, and assigned its uncertainties based on the measured scatter across the five hour dataset. We then compared this average spectrum against the nearest matching M6 template from Bochanski et al. (2007). The data show a small depression near the expected lithium wavelength, potentially consistent with the  $\Delta\lambda \approx 3$  Å line broadening. This feature yields  $\text{EW}_{\text{Li}} = 71_{-13}^{+18}$  mÅ, where the statistical uncertainties are evaluated using a bootstrap resampling technique from the statistical uncertainties in the HIRES spectrum. However, the systematic uncertainty associated with the continuum normalization is likely comparable to the amplitude of the feature; we therefore treat this measurement as a  $2\sigma$  upper limit:  $\text{EW}_{\text{Li}} < 107$  mÅ.

What can be stated with confidence is that lithium is not abundant in the spectrum of TIC 141146667. Figure 5 compares our upper limit against the equivalent width measurements reported by Jeffries et al. (2023) based on the Gaia-ESO spectroscopic survey. If the star were  $\lesssim 20$  Myr old, at its temperature we would expect to see lithium in abundance ( $> 400$  mÅ). Since we do not, we can set an empirical bound on the lithium-derived age of  $t_{\text{Li,emp}} \gtrsim 20$  Myr. The Feiden (2016) lithium isochrones provide a point for theoretical comparison, and suggest that since  $M_K \approx 6.67$  mag,  $t_{\text{Li,th}} \gtrsim 35$  Myr is the theoretical age at which complete depletion occurs in a star with this luminosity (see e.g. Figure 7 from Wood et al. 2023).

*Age: Summary*—The main indicators for the youth of TIC 141146667 are *i*) that it is a complex periodic variable, and *ii*) that it is 1.5 magnitudes brighter (four times more luminous) than main sequence stars of the same color, while showing no indicators for binarity. Being a CPV suggests that the star is young because a previous CPV search unbiased in age found 90% of its detections to be in  $\lesssim 200$  Myr old clusters (Bouma et al. 2024); the remaining 10% were not associated with any coeval population. Similarly, studies of rotation in  $\lesssim 100$  Myr clusters serendipitously found  $\approx 50\text{--}100$  examples of the class (Rebull et al. 2016; Stauffer et al. 2017, 2018; Rebull et al. 2018; Zhan et al. 2019; Rebull et al. 2020; Stauffer et al. 2021; Rebull et al. 2022; Popinchalk et al. 2023), whereas analogous studies of Praesepe and the Hyades did not report any evidence for CPVs in a set of approximately one thousand  $\approx 700$  Myr stars (Rebull et al. 2017; Douglas et al. 2019; Rampalli et al. 2021). Regarding the isochronal age constraint, the Pleiades (112 Myr, Dahm 2015) shows a few stars of equal luminosity and the same temperature, suggesting a photometric isochronal age upper limit  $\lesssim 150$  Myr. The weak lithium absorption suggests an age of at least 20 Myr based on an empirical comparison using Gaia-ESO spectra, or at least 35 Myr based on the Feiden (2016) isochrones. These considerations yield our adopted age range of 35–150 Myr.

## B. DETAILED BEHAVIOR OF H $\alpha$ : MODEL AND IMPLICATIONS

*A model for the time-dynamic H $\alpha$  spectrum*—While Figure 3 shows that clumps of circumstellar material exist around TIC 141146667, there is value in quantifying the exact orbital periods, velocities, and velocity dispersions of these clumps. These quantities can constrain the physical dimensions of the emitting region, and can also clarify whether the spectroscopic period agrees with the photometric period.

Given that a full radiative transfer simulation was outside our scope, we opted to construct a phenomenological model aimed at capturing the emission from the circumstellar material. We did this by fitting each spectral epoch with a multi-component gaussian, after having subtracted the time-average line profile as in Figure 3e. The results of this exercise are shown in Figure 6; details in the implementation and interpretation follow.

To implement this model, we assumed that the “inner” ( $K_{\text{inner}} \approx 2.5 v_{\text{eq}}$ ) clump would be well-fit by a sum of two gaussians because it is visually double-peaked in the raw data from  $\phi = 0.15\text{--}0.35$  and  $\phi = 0.65\text{--}0.85$  (Figure 3b). We assumed that the “outer” ( $K_{\text{outer}} \approx 3.9 v_{\text{eq}}$ ) clump would be better fit by a single gaussian, based on its behavior from  $\phi = 0.6\text{--}0.9$ . Each gaussian component has three free parameters at each spectral epoch: the mean  $\mu$ , standard deviation  $\sigma$ , and amplitude  $A$ . We labeled the inner component’s two gaussians  $i = \{0, 1\}$ , and the single outer component as  $i = 2$ . Given the complexity of the line profile data (Figure 6 left column), the likelihood function for this model is multimodal. We therefore imposed the prior constraints that  $A_i \sim \mathcal{U}[0, 1]$ ,  $\sigma_i/v_{\text{eq}} \sim \mathcal{U}[0, 1]$ , and further assumed  $\mu_i(t) \sim \mathcal{U}[K_{\text{inner}} \sin(\phi(t)) - v_{\text{eq}}, K_{\text{inner}} \sin(\phi(t)) + v_{\text{eq}}]$  for the inner two components, and  $\mu_2(t) \sim \mathcal{U}[K_{\text{outer}} \sin(\phi(t) + \pi) - 2v_{\text{eq}}, K_{\text{outer}} \sin(\phi(t) + \pi) + 2v_{\text{eq}}]$  for the outer component. This prior on the means mitigates multimodality in the likelihood by requiring the mean velocity of each component to be within a one or two  $v_{\text{eq}}$  of the time-variable sinusoid suggested by visual inspection. We fitted each component to the data *independently* using scipy’s non-linear least squares `curve_fit` implementation (Virtanen et al. 2020), and scaled the resulting parameter covariance matrix by a constant factor to match the sample variance of the residuals. The middle columns of Figure 6 show the results; a table of the fitted means, amplitudes, and standard deviations for each component is available upon request.

Caution is required in interpreting this model’s results. At some epochs there are no significant spectral features around any component’s prior. During such epochs, e.g. the “outer” clump at  $\phi = 1.07$ , the model fits noise, not signal. At other times, the



**Figure 6. Time-variable fit to H $\alpha$  line profiles.** *Left column:* Raw spectrum at each epoch  $f_\lambda$  minus the time-averaged spectrum  $f_{(t)}$  (as in Figure 3e). Underplotted sinusoids are not fits; they are meant to guide the eye. *Middle columns:* Model of emission from the inner clump (sum of two gaussians) and the outer clump (single gaussian), plotted over the data. *Right column:* Residual of the left column after subtracting the sum of the two middle columns, leaving variability in the line core. Appendix B discusses the use of this model.

model underfits. For instance, the sudden blue rise near  $\phi=0.2$  is poorly described by a gaussian; the assumed functional form is one of convenience. Finally, the model fits the  $i = \{0, 1\}$ , and  $i = 2$  components independently. At  $\phi=0.0$  and  $1.0$ , Figure 6 suggests that the emission might come from either the inner or outer components. Physically however, at this epoch the inner clump is in transit, and the outer clump is passing behind the star. At  $\phi=0.0$ , the double-peaked emission profile also matches that seen shortly afterward (at  $\phi=0.14$ ) when the inner clump is viewed off-disk. A physical interpretation of the model would therefore discard the outer clump results at this particular epoch, because its emission would be blocked by the star.

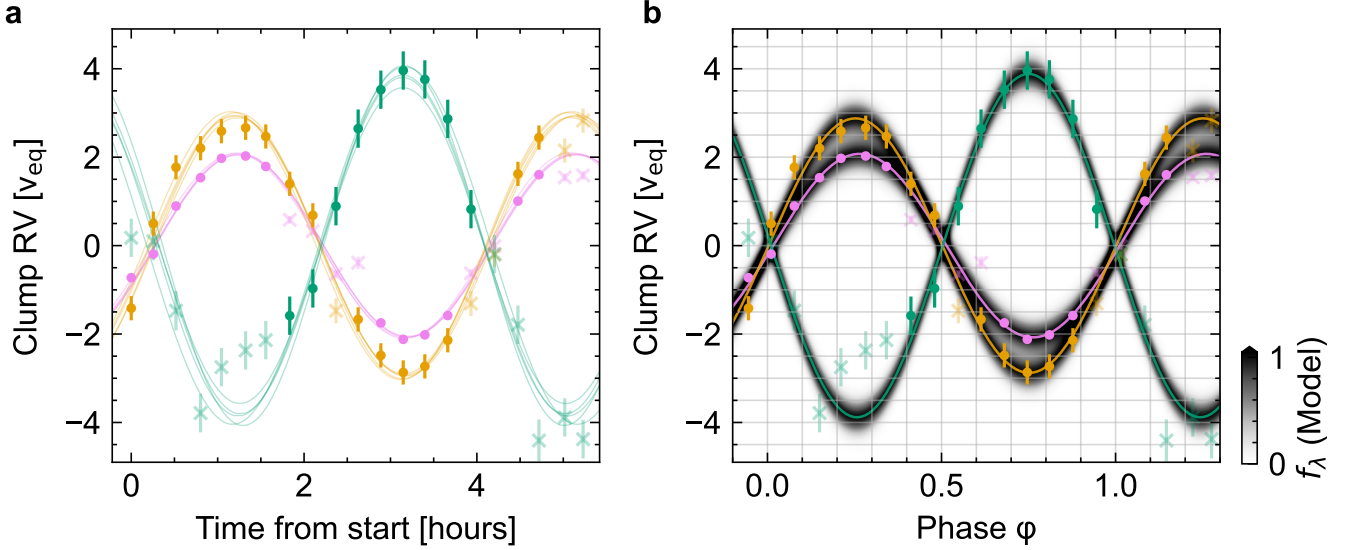


**Figure 7. a,** Orbits fit to mean radial velocities (RVs) extracted from H $\alpha$  profile fits in Figure 6. Radial velocities on the vertical axis are in units of the equatorial velocity,  $v_{\text{eq}}=130 \text{ km s}^{-1}$ . Each marker denotes the best-fit gaussian mean at a given epoch. Solid circles were adopted in the fits; transparent X markers were excluded due to reliability concerns (see text). The inner double-peaked clump is shown in violet and orange; the outer clump is shown in green. Five model draws from each posterior probability distribution are plotted. **b,** Idealized emissivity from mean model fits in Panel a, assuming a constant emission amplitude and velocity width  $\sigma=0.25 v_{\text{eq}}$  and neglecting eclipses.

Accounting for these caveats, we used the best-fit parameters from the multi-gaussian model to quantify the orbital periods and velocity semi-amplitudes of the clumps. Figure 7a shows the results assuming circular orbits; considering the Bayesian information criterion, we found no reason to prefer eccentric orbits. By visually inspecting Figure 6, we excluded epochs where our gaussian profile fitting failed to either detect or else adequately represent the circumstellar emission. We then used NumPyro to sample the Gaussian likelihood for a circular orbit with the NUTS algorithm (Phan et al. 2019). We used the measurement uncertainties from each estimated mean radial velocity value and included an additional jitter term in quadrature. This procedure yielded orbital periods and semi-amplitudes of  $P_0=3.92 \pm 0.03 \text{ hr}$ ,  $K_0/v_{\text{eq}}=2.07 \pm 0.04$ ;  $P_1=3.92 \pm 0.06 \text{ hr}$ ,  $K_1/v_{\text{eq}}=2.88 \pm 0.10$ ; and  $P_2=3.88 \pm 0.20 \text{ hr}$ ,  $K_2/v_{\text{eq}}=3.88 \pm 0.25$ . The periods for the inner double-peaked clump are therefore consistent with the photometric  $3.930 \pm 0.001 \text{ hr}$  period within a precision of two minutes. The “period” for the outer clump is ambiguous because the H $\alpha$  data only support the idea of a periodic orbit of material well-fit by gaussian emission from  $\phi \approx 0.5-1.0$ . From  $\phi=0-0.2$ , there is no detectable emission, and from  $\phi=0.2-0.4$ , the emission spans  $1-4 v_{\text{eq}}$  without taking a clear gaussian shape. While the outer-most edge of this  $\phi=0.2-0.4$  emission provides a plausible match to the expectation of a circular orbit, the idea of invoking a particular functional form for this component seems fine-tuned. We instead emphasize that although this emission is present, its variability in time is inconsistent with the idea of a stable clump of material. Additional observations would be needed to conclusively determine whether or not this component of the system is long-lived.

For Figure 7b, we then used the mean orbits from Figure 7a to generate sinusoidal-in-time gaussians, similar to the observations. We assumed a constant emission amplitude and velocity width  $\sigma=0.25 v_{\text{eq}}$  for this exercise, and normalized each gaussian to unit amplitude; the colorbar in Figure 7b thus masks the non-physical additive contribution near the zero-crossing of velocity. Compared to the behavior of the data at  $\phi=0.2-0.5$  (Figure 3), this is highly idealized. Nonetheless, this exercise indicates that the transit of the inner clump lasts  $\approx 22\%$  of each cycle, with a slight asymmetry around  $\phi=0$ .

*Physical dimensions of emitting region*—The H $\alpha$  velocity widths in Figure 6 constrain the size of the emitting region via the condition for rigid corotation. Consider a clump in cylindrical coordinates with arbitrary radial extent  $r$ , azimuthal extent  $\ell$ , and height  $z$ . A range of shapes, including an “arc” with  $\ell \gg r$ , a “spoke” with  $r \gg \ell$ , and a “blob” with  $r \approx \ell \approx z$  are all a priori possible. However, at quadrature, the observed velocity width of emission is sensitive to the radial extent of the circumstellar material. At mid-transit, the observed velocity width is sensitive to the azimuthal extent. An arc configuration would minimize the observed velocity width  $\sigma$  at quadrature, and maximize it during transit, with  $\gtrsim 100 \text{ km s}^{-1}$  variations in between. Since this is not observed, the arc geometry, and by a similar argument the spoke geometry, can be discarded.

At quadrature, the inner clumps show  $\sigma_i \approx 0.24 v_{\text{eq}}$ , implying that 68% of the emission comes from a volume with length in the radial dimension  $r_i=2\sigma_i/\Omega=0.48 R_*$ , and that 95% of the emission comes from within  $0.96 R_*$ . These values have relative uncertainties of  $\approx 5\%$ , based on the uncertainties in the measured velocity dispersions. The two inner clumps are centered at orbital distances of  $2.07 R_*$  and  $2.88 R_*$ . There is therefore physical overlap in their spatial distributions. These two clumps could



in fact be a single clump with an optically thick  $H\alpha$  line core. Regardless, the implication is that the full length in the radial dimension of these two inner emitting clumps is approximately equal to the star's diameter. At mid-transit, these inner clumps have a similar velocity dispersion, although with greater uncertainty due to the differences between the  $\phi=0$  and  $\phi=1$  transits (see Figure 6). This suggests a  $1\sigma$  emission contour in the azimuthal dimension with a length of  $\ell \approx 0.5 R_*$ .

The vertical height of the emitting region is less constrained because the system is consistent with being viewed edge-on. However, one possible constraint follows by assuming that the TESS transit depth scales with the projected  $H\alpha$  emission area  $\ell z$ . More specifically, one can evaluate an “effective area” blocked by a two-dimensional gaussian blob passing over a star by integrating the local gaussian weight over the stellar surface. For instance, if  $\ell \approx z \approx 0.24 R_*$ , then  $\iint \exp(-x^2/2\sigma_x^2 - y^2/2\sigma_y^2) dx dy$  suggests 11.5% of the star being “blocked”, a geometric factor which would need to be in turn multiplied by an unknown opacity factor to produce the observed transit depth ( $\delta \approx 5\%$ ). There is a degeneracy between  $z$  and this opacity factor; larger vertical heights are allowed for lower optical depths in absorption, and vice-versa. This constraint also implicitly assumes that the optically thick material is well-mixed with the hydrogen, which may not be accurate.

### C. PROPERTIES OF THE PLASMA AND MAGNETOSPHERIC ENVIRONMENT

The hydrogen number density, plasma temperature, and magnetic field strength inside the clumps can be estimated from the available data. The following order-of-magnitude calculations assume a simple uniform-density plasma in a spherical geometry: more careful considerations of radiative transfer are a worthy topic for future work.

Circumstellar  $H\alpha$  emission could come either from resonant scattering of stellar  $H\alpha$  photons, or from radiative recombination. We neglect scattering because Figure 3 shows the circumstellar  $H\alpha$  emission varying by a factor of  $\approx 5$  while the chromospheric line core is stable. The volume emissivity under case B recombination can be written

$$j_{H\alpha} = n_e n_p \alpha_{H\alpha}^{\text{eff}} h\nu_{H\alpha}, \quad (\text{C1})$$

where  $n_e$  and  $n_p$  are the electron and proton densities, and  $\alpha_{H\alpha}^{\text{eff}}$  is the effective recombination coefficient, defined to include all recombination routes that produce an  $H\alpha$  photon. For hydrogen with temperatures between 1,000-10,000 K,  $\alpha_{H\alpha}^{\text{eff}}$  is typically  $10^{-12}$  to  $10^{-13} \text{ cm}^3 \text{ s}^{-1}$  (Hummer & Storey 1987; Draine 2011). Neglecting atoms other than hydrogen, we can assume an ionization fraction  $x$ , such that  $n_e = n_p = x n_H$ , for  $n_H$  the hydrogen number density. Let  $L_{H\alpha} = j_{H\alpha} V$ , for  $V$  the volume of the emitting hydrogen. The luminosity of circumstellar hydrogen emission,  $L_{H\alpha}$ , is an observable: our SED fitting routine yields  $L_* \approx 0.012 L_\odot$ , which implies that the stellar  $H\alpha$  line radiates at  $\approx 1.0 \times 10^{28} \text{ erg s}^{-1}$ . The luminosity of the clumps  $L_{H\alpha}$  are of order one tenth that of the star. If we approximate the emitting volume as a homogeneous sphere of radius  $r$ , we can write

$$n_H = 1 \cdot 10^{11} \text{ cm}^{-3} \left( \frac{0.5}{x} \right) \left( \frac{L_{H\alpha}}{10^{27} \text{ erg s}^{-1}} \frac{10^{-13} \text{ cm}^3 \text{ s}^{-1}}{\alpha_{H\alpha}^{\text{eff}}} \right)^{1/2} \left( \frac{0.1 R_\odot}{r} \right)^{3/2}. \quad (\text{C2})$$

For a uniform density clump, this suggests a total gas mass of  $M_{\text{gas}} \approx 2 \times 10^{17} \text{ g}$ , which is similar to masses derived for plasma clumps around other cool stars (Villareal D'Angelo et al. 2019). We emphasize that Equation C2 is intended to provide only an order of magnitude estimate for the number density implied by the observed  $H\alpha$  emission. In detail, the effective recombination rate and the ionization fraction each vary with density and temperature; a more thorough estimate would iteratively solve the equations of detailed balance and radiative transfer (e.g. Figure 8 of Collier Cameron & Robinson 1989), and potentially also consider departures from local thermodynamic equilibrium.

Finally, a constraint on the magnetic field strength at the site of the clump follows from the requirement that the magnetic pressure exceed the thermal pressure,  $B_c^2/8\pi > n_H kT$ . Although we do not know the exact plasma temperature, if it were significantly beyond 1,000-10,000 K, we would either fully ionize the hydrogen, or not ionize enough of it. The field strength at the clump must therefore exceed

$$B_c \gtrsim 1 \text{ G} \left( \frac{n_H}{1 \times 10^{11} \text{ cm}^{-3}} \frac{T}{3000 \text{ K}} \right)^{1/2}. \quad (\text{C3})$$

Given that the average surface magnetic field strengths of low-mass stars have been measured to span hundreds to thousands of Gauss (Donati & Landstreet 2009; Kochukhov 2021; Reiners et al. 2022), this bound is easily met at orbital distances of  $2-4 R_*$ .

### D. UPPER AND LOWER BOUNDS ON DUST

The material's composition – either pure plasma, or a dusty plasma – is not known. The idea of dust being present seems plausible given observations of chromatic transits in analogous objects (Tanimoto et al. 2020; Günther et al. 2022; Koen 2023). However, this scenario is highly constrained. An upper limit on the amount of hot dust follows from the lack of an infrared excess. A lower limit follows if one assumes that most of the broadband optical depth comes from dust absorption and scattering, rather than any radiative processes associated with the plasma.

Regarding the upper limit, Figure 4 shows the SED. While AllWISE (Cutri et al. 2021) yielded a confident W3 detection ( $9.8\sigma$ ) consistent with the photospheric extrapolation from bluer bandpasses, the W4 extraction yielded only a marginal indication ( $1.7\sigma$ )

of detectable flux. Similar to other CPVs (Stauffer et al. 2017; Bouma et al. 2024), the photometric uncertainties from WISE W1 and W2 allow at most a  $\lesssim 2\%$  excess at  $3\text{--}5\text{ }\mu\text{m}$  relative to the stellar photosphere, and a  $\lesssim 5\%$  excess at  $10\text{ }\mu\text{m}$  (W3). To estimate the implied mass bound, we assume a dust temperature  $T_d=1500\text{ K}$ , typical for dust near the star (see Zhan et al. 2019 for discussion regarding dust sublimation). We then treat emission from the dust and star as Planck functions, and require  $L_d < fL_*$ , where the factor  $f$  is set by the photometric precision of WISE and  $L_d$  is the bolometric dust luminosity. Given the reported uncertainties, we numerically find  $f < 6 \cdot 10^{-3}$ . From the Stefan-Boltzmann law we can then write  $A_d < f(T_*/T_d)^4 Q_{\text{em}}^{-1} (4\pi R_*)^2$ , for  $A_d$  the total emitting surface area of the dust, and  $Q_{\text{em}}$  an emission efficiency parameter. Converting this constraint to a dust mass requires an assumption regarding the grain properties. We assume a grain density  $\rho_d=3\text{ g cm}^{-3}$  typical for silicate grains, a fixed grain size  $a=1\text{ }\mu\text{m}$ , and no self-absorption. This enables the assumption that  $A_d = N\pi a^2$ , for  $N$  the total number of dust grains. This in turn yields an upper limit on the dust mass of

$$M_{\text{dust}} \lesssim 4 \cdot 10^{17} \text{ g} \left( \frac{f}{6 \cdot 10^{-3}} \right) \left( \frac{T_*}{3000 \text{ K}} \frac{1500 \text{ K}}{T_d} \right)^4 \left( \frac{Q_{\text{em}}}{1} \right)^{-1} \left( \frac{R_*}{0.4 R_\odot} \right)^2 \left( \frac{a}{1 \mu\text{m}} \right) \left( \frac{\rho_d}{3 \text{ g cm}^{-3}} \right). \quad (\text{D4})$$

The analogous lower limit follows from requiring the optical depth from absorption and scattering  $\tau$  to be at least unity. The optical depth can be written  $\tau = n\sigma\ell$ , where  $\sigma$  is the cross-section,  $n$  is the number density,  $\ell$  is the path length. For spherical dust grains in the optical,  $\sigma = Q_{\text{ext}}\pi a^2$ , where  $Q_{\text{ext}}$  is the extinction efficiency parameter, tabulated e.g. by Croll et al. (2014) in their Figure 13. Sanderson et al. (2023) calculated the relevant cloud mass for this problem assuming a spherical dust clump of size  $r$ , and they found

$$M_{\text{dust}} \gtrsim 2 \cdot 10^{15} \text{ g} \left( \frac{\tau}{1} \right) \left( \frac{Q_{\text{ext}}}{3} \right)^{-1} \left( \frac{r}{0.1 R_*} \frac{R_*}{0.4 R_\odot} \right)^2 \left( \frac{a}{1 \mu\text{m}} \right) \left( \frac{\rho_d}{3 \text{ g cm}^{-3}} \right). \quad (\text{D5})$$

Three relevant objects for comparison include solar prominences, planetesimals, and comets. Prominences of the Sun have gas masses of  $10^{14}\text{--}10^{16}\text{ g}$  (Vial & Engvold 2015). A planetesimal of mass  $\approx 10^{15}\text{ g}$  with a bulk density of  $1\text{ g cm}^{-3}$  would have a diameter of order one kilometer. Halley’s comet has a mass of order  $10^{17}\text{ g}$  (Rickman 1989), of which  $\sim 10^{14}\text{ g}$  is shed per orbit, most of which inspirals toward the Sun due to Poynting-Robertson drag.

To summarize, if dust is responsible for the broadband variability of CPVs, it would need to be concentrated in clumps with masses in the range of  $10^{15}\text{--}10^{17}\text{ g}$ . Given  $M_{\text{gas}} \approx 2 \times 10^{17}\text{ g}$  from Appendix C, the allowed dust masses imply  $M_{\text{gas}}/M_{\text{dust}}$  ranges of 1–100. More careful measurements of this ratio—in particular by inferring the dust mass through high precision infrared spectrophotometry—could provide a path for distinguishing the scenario of a trapped stellar outflow from an accumulation of externally-sourced material. While there are several plausible external sources, feeding through a low-mass disk in particular cannot be ruled out based on typical disk depletion times (Haisch et al. 2001). Observations of infrared excesses and accretion signatures in low-mass stars tens of millions of years old suggest a broad lifetime distribution for such disks (Silverberg et al. 2020; Lee et al. 2020; Gaidos et al. 2022; Pfalzner & Dincer 2024).

## REFERENCES

- Allard, F., Homeier, D., & Freytag, B. 2012, *Philosophical Transactions of the Royal Society A: Mathematical, Physical and Engineering Sciences*, 370, 2765, doi: [10.1098/rsta.2011.0269](https://doi.org/10.1098/rsta.2011.0269)
- Astropy Collaboration, Robitaille, T. P., Tollerud, E. J., et al. 2013, *A&A*, 558, A33, doi: [10.1051/0004-6361/201322068](https://doi.org/10.1051/0004-6361/201322068)
- Astropy Collaboration, Price-Whelan, A. M., Sipőcz, B. M., et al. 2018, *AJ*, 156, 123, doi: [10.3847/1538-3881/aabc4f](https://doi.org/10.3847/1538-3881/aabc4f)
- Astropy Collaboration, Price-Whelan, A. M., Lim, P. L., et al. 2022, *ApJ*, 935, 167, doi: [10.3847/1538-4357/ac7c74](https://doi.org/10.3847/1538-4357/ac7c74)
- Bagenal, F., & Sullivan, J. D. 1981, *J. Geophys. Res.*, 86, 8447, doi: [10.1029/JA086iA10p08447](https://doi.org/10.1029/JA086iA10p08447)
- Barnes, J. R., Collier Cameron, A., James, D. J., & Donati, J. F. 2000, *MNRAS*, 314, 162, doi: [10.1046/j.1365-8711.2000.03237.x](https://doi.org/10.1046/j.1365-8711.2000.03237.x)
- Bellotti, S., Morin, J., Lehmann, L. T., et al. 2024, *A&A*, 686, A66, doi: [10.1051/0004-6361/202348043](https://doi.org/10.1051/0004-6361/202348043)
- Berry, I. D., Owocki, S. P., Shultz, M. E., & ud-Doula, A. 2022, *MNRAS*, 511, 4815, doi: [10.1093/mnras/stac322](https://doi.org/10.1093/mnras/stac322)
- Bhatti, W., Bouma, L., Joshua, et al. 2021, *waqasbhatti/astrobase: astrobase v0.5.3, v0.5.3, Zenodo, Zenodo*, doi: [10.5281/zenodo.1011188](https://doi.org/10.5281/zenodo.1011188)
- Bildsten, L., Brown, E. F., Matzner, C. D., & Ushomirsky, G. 1997, *ApJ*, 482, 442, doi: [10.1086/304151](https://doi.org/10.1086/304151)
- Bochanski, J. J., West, A. A., Hawley, S. L., & Covey, K. R. 2007, *AJ*, 133, 531, doi: [10.1086/510240](https://doi.org/10.1086/510240)
- Bouma, L. G., Jayaraman, R., Rappaport, S., et al. 2024, *AJ*, 167, 38, doi: [10.3847/1538-3881/ad0c4c](https://doi.org/10.3847/1538-3881/ad0c4c)
- Bouma, L. G., Winn, J. N., Ricker, G. R., et al. 2020, *AJ*, 160, 86, doi: [10.3847/1538-3881/ab9e73](https://doi.org/10.3847/1538-3881/ab9e73)
- Briceño, C., Calvet, N., Hernández, J., et al. 2019, *AJ*, 157, 85, doi: [10.3847/1538-3881/aaf79b](https://doi.org/10.3847/1538-3881/aaf79b)
- Brown, B. P., Oishi, J. S., Vasil, G. M., Lecoanet, D., & Burns, K. J. 2020, *ApJL*, 902, L3, doi: [10.3847/2041-8213/abb9a4](https://doi.org/10.3847/2041-8213/abb9a4)

Time [BJD <sub>TDB</sub> ]	RV (km s <sup>-1</sup> )	$\sigma_{RV}$ (km s <sup>-1</sup> )
2460357.954919	2.73	5.86
2460357.965845	-4.40	2.37
2460357.976770	-0.19	2.64
2460357.987698	3.84	2.87
2460357.998619	7.53	7.53
2460358.009538	-1.98	1.44
2460358.020462	1.02	1.21
2460358.031383	0.64	7.03
2460358.042306	-2.91	2.71
2460358.053228	8.93	6.75
2460358.064154	5.95	8.84
2460358.075075	-2.25	3.06
2460358.085996	1.84	1.34
2460358.096918	2.41	8.24
2460358.107839	-7.04	3.94
2460358.118760	-2.24	3.07
2460358.129683	-2.83	7.55
2460358.140606	-0.59	2.26
2460358.151527	1.84	2.91
2460358.162448	4.54	3.95
2460358.173368	6.21	12.14

**Table 2.** TIC 141146667 radial velocities relative to the systemic velocity based on the 7699 Å resonance line and TiO bandheads.

- 733 Callingham, J. R., Vedantham, H. K., Shimwell, T. W., et al. 2021,  
734 Nature Astronomy, 5, 1233, doi: [10.1038/s41550-021-01483-0](https://doi.org/10.1038/s41550-021-01483-0)
- 735 Cang, T. Q., Petit, P., Donati, J. F., & Folsom, C. P. 2021, A&A,  
736 654, A42, doi: [10.1051/0004-6361/202141975](https://doi.org/10.1051/0004-6361/202141975)
- 737 Cang, T. Q., Petit, P., Donati, J. F., et al. 2020, A&A, 643, A39,  
738 doi: [10.1051/0004-6361/202037693](https://doi.org/10.1051/0004-6361/202037693)
- 739 Chen, Y., Girardi, L., Bressan, A., et al. 2014, MNRAS, 444, 2525,  
740 doi: [10.1093/mnras/stu1605](https://doi.org/10.1093/mnras/stu1605)
- 741 Chubak, C., Marcy, G., Fischer, D. A., et al. 2012, arXiv e-prints,  
742 arXiv:1207.6212, doi: [10.48550/arXiv.1207.6212](https://doi.org/10.48550/arXiv.1207.6212)
- 743 Collier Cameron, A., & Robinson, R. D. 1989, MNRAS, 236, 57,  
744 doi: [10.1093/mnras/236.1.57](https://doi.org/10.1093/mnras/236.1.57)
- 745 Collier Cameron, A., & Woods, J. A. 1992, MNRAS, 258, 360,  
746 doi: [10.1093/mnras/258.2.360](https://doi.org/10.1093/mnras/258.2.360)
- 747 Croll, B., Rappaport, S., DeVore, J., et al. 2014, ApJ, 786, 100,  
748 doi: [10.1088/0004-637X/786/2/100](https://doi.org/10.1088/0004-637X/786/2/100)
- 749 Cutri, R. M., Wright, E. L., Conrow, T., et al. 2021, VizieR Online  
750 Data Catalog, II/328
- 751 Dahm, S. E. 2015, ApJ, 813, 108,  
752 doi: [10.1088/0004-637X/813/2/108](https://doi.org/10.1088/0004-637X/813/2/108)
- 753 Daley-Yates, S., & Jardine, M. M. 2024, MNRAS, 534, 621,  
754 doi: [10.1093/mnras/stae2131](https://doi.org/10.1093/mnras/stae2131)
- 755 Daley-Yates, S., Jardine, M. M., & Johnston, C. D. 2023, MNRAS,  
756 526, 1646, doi: [10.1093/mnras/stad2752](https://doi.org/10.1093/mnras/stad2752)
- 757 Donati, J.-F., Forveille, T., Collier Cameron, A., et al. 2006,  
758 Science, 311, 633, doi: [10.1126/science.1121102](https://doi.org/10.1126/science.1121102)
- 759 Donati, J. F., & Landstreet, J. D. 2009, ARA&A, 47, 333,  
760 doi: [10.1146/annurev-astro-082708-101833](https://doi.org/10.1146/annurev-astro-082708-101833)
- 761 Donati, J. F., Mengel, M., Carter, B. D., et al. 2000, MNRAS, 316,  
762 699, doi: [10.1046/j.1365-8711.2000.03570.x](https://doi.org/10.1046/j.1365-8711.2000.03570.x)
- 763 Douglas, S. T., Curtis, J. L., Agüeros, M. A., et al. 2019, ApJ, 879,  
764 100, doi: [10.3847/1538-4357/ab2468](https://doi.org/10.3847/1538-4357/ab2468)
- 765 Draine, B. T. 2011, Physics of the Interstellar and Intergalactic  
766 Medium
- 767 Dressing, C. D., & Charbonneau, D. 2015, ApJ, 807, 45,  
768 doi: [10.1088/0004-637X/807/1/45](https://doi.org/10.1088/0004-637X/807/1/45)
- 769 Dunstone, N. J., Collier Cameron, A., Barnes, J. R., & Jardine, M.  
770 2006, MNRAS, 373, 1308,  
771 doi: [10.1111/j.1365-2966.2006.11128.x](https://doi.org/10.1111/j.1365-2966.2006.11128.x)
- 772 Feiden, G. A. 2016, A&A, 593, A99,  
773 doi: [10.1051/0004-6361/201527613](https://doi.org/10.1051/0004-6361/201527613)
- 774 Feinstein, A. D., Montet, B. T., Ansdell, M., et al. 2020, AJ, 160,  
775 219, doi: [10.3847/1538-3881/abac0a](https://doi.org/10.3847/1538-3881/abac0a)
- 776 Ferreira, J. M. 2000, MNRAS, 316, 647,  
777 doi: [10.1046/j.1365-8711.2000.03540.x](https://doi.org/10.1046/j.1365-8711.2000.03540.x)
- 778 France, K., Loyd, R. O. P., Youngblood, A., et al. 2016, ApJ, 820,  
779 89, doi: [10.3847/0004-637X/820/2/89](https://doi.org/10.3847/0004-637X/820/2/89)
- 780 Gagné, J., Mamajek, E. E., Malo, L., et al. 2018, ApJ, 856, 23,  
781 doi: [10.3847/1538-4357/aaae09](https://doi.org/10.3847/1538-4357/aaae09)
- 782 Gaia Collaboration, Brown, A. G. A., Vallenari, A., et al. 2018,  
783 A&A, 616, A1, doi: [10.1051/0004-6361/201833051](https://doi.org/10.1051/0004-6361/201833051)
- 784 Gaia Collaboration, Vallenari, A., Brown, A. G. A., et al. 2023,  
785 A&A, 674, A1, doi: [10.1051/0004-6361/202243940](https://doi.org/10.1051/0004-6361/202243940)
- 786 Gaidos, E., Mann, A. W., Rojas-Ayala, B., et al. 2022, MNRAS,  
787 514, 1386, doi: [10.1093/mnras/stac1433](https://doi.org/10.1093/mnras/stac1433)
- 788 Gray, D. F. 2008, The Observation and Analysis of Stellar  
789 Photospheres

- Green, G. 2018, *The Journal of Open Source Software*, 3, 695, doi: [10.21105/joss.00695](https://doi.org/10.21105/joss.00695)
- Green, G. M., Schlafly, E., Zucker, C., Speagle, J. S., & Finkbeiner, D. 2019, *ApJ*, 887, 93, doi: [10.3847/1538-4357/ab5362](https://doi.org/10.3847/1538-4357/ab5362)
- Günther, M. N., Berardo, D. A., Ducrot, E., et al. 2022, *AJ*, 163, 144, doi: [10.3847/1538-3881/ac503c](https://doi.org/10.3847/1538-3881/ac503c)
- Haisch, Jr., K. E., Lada, E. A., & Lada, C. J. 2001, *ApJL*, 553, L153, doi: [10.1086/320685](https://doi.org/10.1086/320685)
- Hayashi, C., & Nakano, T. 1963, *Progress of Theoretical Physics*, 30, 460, doi: [10.1143/PTP.30.460](https://doi.org/10.1143/PTP.30.460)
- Howard, A. W., Johnson, J. A., Marcy, G. W., et al. 2010, *ApJ*, 721, 1467, doi: [10.1088/0004-637X/721/2/1467](https://doi.org/10.1088/0004-637X/721/2/1467)
- Hummer, D. G., & Storey, P. J. 1987, *MNRAS*, 224, 801, doi: [10.1093/mnras/224.3.801](https://doi.org/10.1093/mnras/224.3.801)
- Hunt, E. L., & Reffert, S. 2024, *A&A*, 686, A42, doi: [10.1051/0004-6361/202348662](https://doi.org/10.1051/0004-6361/202348662)
- Hunter, J. D., et al. 2007, *Computing in science and engineering*, 9, 90
- Husser, T. O., Wende-von Berg, S., Dreizler, S., et al. 2013, *A&A*, 553, A6, doi: [10.1051/0004-6361/201219058](https://doi.org/10.1051/0004-6361/201219058)
- Jardine, M., Collier Cameron, A., & Donati, J. F. 2002, *MNRAS*, 333, 339, doi: [10.1046/j.1365-8711.2002.05394.x](https://doi.org/10.1046/j.1365-8711.2002.05394.x)
- Jeffries, R. D., Jackson, R. J., Wright, N. J., et al. 2023, *MNRAS*, 523, 802, doi: [10.1093/mnras/stad1293](https://doi.org/10.1093/mnras/stad1293)
- Jenkins, J. M., Twicken, J. D., McCauliff, S., et al. 2016, in *Society of Photo-Optical Instrumentation Engineers (SPIE) Conference Series*, Vol. 9913, *Software and Cyberinfrastructure for Astronomy IV*, ed. G. Chiozzi & J. C. Guzman, 99133E, doi: [10.1117/12.2233418](https://doi.org/10.1117/12.2233418)
- Johns-Krull, C. M., Prato, L., McLane, J. N., et al. 2016, *ApJ*, 830, 15, doi: [10.3847/0004-637X/830/1/15](https://doi.org/10.3847/0004-637X/830/1/15)
- Kanodia, S., & Wright, J. 2018, *Research Notes of the American Astronomical Society*, 2, 4, doi: [10.3847/2515-5172/aaa4b7](https://doi.org/10.3847/2515-5172/aaa4b7)
- Kaur, S., Viganò, D., Béjar, V. J. S., et al. 2024, *A&A*, 691, L17, doi: [10.1051/0004-6361/202452037](https://doi.org/10.1051/0004-6361/202452037)
- Kislyakova, K. G., Fossati, L., Johnstone, C. P., et al. 2018, *ApJ*, 858, 105, doi: [10.3847/1538-4357/aabae4](https://doi.org/10.3847/1538-4357/aabae4)
- Kochukhov, O. 2021, *A&A Rv*, 29, 1, doi: [10.1007/s00159-020-00130-3](https://doi.org/10.1007/s00159-020-00130-3)
- Kochukhov, O., & Lavail, A. 2017, *ApJL*, 835, L4, doi: [10.3847/2041-8213/835/1/L4](https://doi.org/10.3847/2041-8213/835/1/L4)
- Kochukhov, O., Lundin, A., Romanyuk, I., & Kudryavtsev, D. 2011, *ApJ*, 726, 24, doi: [10.1088/0004-637X/726/1/24](https://doi.org/10.1088/0004-637X/726/1/24)
- Koen, C. 2021, *A&A*, 647, L1, doi: [10.1051/0004-6361/202140400](https://doi.org/10.1051/0004-6361/202140400)
- . 2023, *MNRAS*, 518, 2921, doi: [10.1093/mnras/stac3276](https://doi.org/10.1093/mnras/stac3276)
- Krtićka, J., Mikulášek, Z., Kurfürst, P., & Oksala, M. E. 2022, *A&A*, 659, A37, doi: [10.1051/0004-6361/202141997](https://doi.org/10.1051/0004-6361/202141997)
- Lee, J., Song, I., & Murphy, S. 2020, *MNRAS*, 494, 62, doi: [10.1093/mnras/staa689](https://doi.org/10.1093/mnras/staa689)
- Leitzinger, M., Odert, P., Zaqarashvili, T. V., et al. 2016, *MNRAS*, 463, 965, doi: [10.1093/mnras/stw1922](https://doi.org/10.1093/mnras/stw1922)
- Marigo, P., Girardi, L., Bressan, A., et al. 2008, *A&A*, 482, 883, doi: [10.1051/0004-6361:20078467](https://doi.org/10.1051/0004-6361:20078467)
- Mikulášek, Z., Krtićka, J., Shultz, M. E., et al. 2020, in *Stellar Magnetism: A Workshop in Honour of the Career and Contributions of John D. Landstreet*, ed. G. Wade, E. Alecian, D. Bohlender, & A. Sigut, Vol. 11, 46–53, doi: [10.48550/arXiv.1912.04121](https://doi.org/10.48550/arXiv.1912.04121)
- Nakajima, R. 1985, *Ap&SS*, 116, 285, doi: [10.1007/BF00653783](https://doi.org/10.1007/BF00653783)
- Open-AI. 2025, ChatGPT, Model o3; Conversational AI model used for editing manuscript and generating testable code; the author wrote all of the original manuscript text. <https://chat.openai.com/>
- Pecaut, M. J., & Mamajek, E. E. 2016, *MNRAS*, 461, 794, doi: [10.1093/mnras/stw1300](https://doi.org/10.1093/mnras/stw1300)
- Petit, V., Owocki, S. P., Wade, G. A., et al. 2013, *MNRAS*, 429, 398, doi: [10.1093/mnras/sts344](https://doi.org/10.1093/mnras/sts344)
- Pfalzner, S., & Dincer, F. 2024, *ApJ*, 963, 122, doi: [10.3847/1538-4357/ad1bef](https://doi.org/10.3847/1538-4357/ad1bef)
- Phan, D., Pradhan, N., & Jankowiak, M. 2019, *arXiv e-prints*, arXiv:1912.11554, doi: [10.48550/arXiv.1912.11554](https://doi.org/10.48550/arXiv.1912.11554)
- Popinchalk, M., Faherty, J. K., Curtis, J. L., et al. 2023, *ApJ*, 945, 114, doi: [10.3847/1538-4357/acb055](https://doi.org/10.3847/1538-4357/acb055)
- Rackham, B. V., Apai, D., & Giampapa, M. S. 2018, *ApJ*, 853, 122, doi: [10.3847/1538-4357/aaa08c](https://doi.org/10.3847/1538-4357/aaa08c)
- Rampalli, R., Agüeros, M. A., Curtis, J. L., et al. 2021, *ApJ*, 921, 167, doi: [10.3847/1538-4357/ac0c1e](https://doi.org/10.3847/1538-4357/ac0c1e)
- Randich, S., Tognelli, E., Jackson, R., et al. 2018, *A&A*, 612, A99, doi: [10.1051/0004-6361/201731738](https://doi.org/10.1051/0004-6361/201731738)
- Ratzenböck, S., Großschedl, J. E., Möller, T., et al. 2023, *A&A*, 677, A59, doi: [10.1051/0004-6361/202243690](https://doi.org/10.1051/0004-6361/202243690)
- Reach, W. T., Lisse, C., von Hippel, T., & Mullally, F. 2009, *ApJ*, 693, 697, doi: [10.1088/0004-637X/693/1/697](https://doi.org/10.1088/0004-637X/693/1/697)
- Rebull, L. M., Stauffer, J. R., Cody, A. M., et al. 2020, *AJ*, 159, 273, doi: [10.3847/1538-3881/ab893c](https://doi.org/10.3847/1538-3881/ab893c)
- . 2018, *AJ*, 155, 196, doi: [10.3847/1538-3881/aab605](https://doi.org/10.3847/1538-3881/aab605)
- Rebull, L. M., Stauffer, J. R., Hillenbrand, L. A., et al. 2017, *ApJ*, 839, 92, doi: [10.3847/1538-4357/aa6aa4](https://doi.org/10.3847/1538-4357/aa6aa4)
- . 2022, *AJ*, 164, 80, doi: [10.3847/1538-3881/ac75f1](https://doi.org/10.3847/1538-3881/ac75f1)
- Rebull, L. M., Stauffer, J. R., Bouvier, J., et al. 2016, *AJ*, 152, 114, doi: [10.3847/0004-6256/152/5/114](https://doi.org/10.3847/0004-6256/152/5/114)
- Redfield, S., Batalha, N., Benneke, B., et al. 2024, *arXiv e-prints*, arXiv:2404.02932, doi: [10.48550/arXiv.2404.02932](https://doi.org/10.48550/arXiv.2404.02932)
- Reiners, A., Shulyak, D., Käpylä, P. J., et al. 2022, *A&A*, 662, A41, doi: [10.1051/0004-6361/202243251](https://doi.org/10.1051/0004-6361/202243251)
- Ribas, Á., Bouy, H., & Merín, B. 2015, *A&A*, 576, A52, doi: [10.1051/0004-6361/201424846](https://doi.org/10.1051/0004-6361/201424846)



- Ricker, G. R., Winn, J. N., Vanderspek, R., et al. 2015, *Journal of Astronomical Telescopes, Instruments, and Systems*, 1, 014003, doi: [10.1117/1.JATIS.1.1.014003](https://doi.org/10.1117/1.JATIS.1.1.014003)
- Rickman, H. 1989, *Advances in Space Research*, 9, 59, doi: [10.1016/0273-1177\(89\)90241-X](https://doi.org/10.1016/0273-1177(89)90241-X)
- Sanderson, H., Jardine, M., Collier Cameron, A., Morin, J., & Donati, J. F. 2023, *MNRAS*, 518, 4734, doi: [10.1093/mnras/stac3302](https://doi.org/10.1093/mnras/stac3302)
- Shultz, M. E., Wade, G. A., Rivinius, T., et al. 2018, *MNRAS*, 475, 5144, doi: [10.1093/mnras/sty103](https://doi.org/10.1093/mnras/sty103)
- Shulyak, D., Reiners, A., Nagel, E., et al. 2019, *A&A*, 626, A86, doi: [10.1051/0004-6361/201935315](https://doi.org/10.1051/0004-6361/201935315)
- Silverberg, S. M., Wisniewski, J. P., Kuchner, M. J., et al. 2020, *ApJ*, 890, 106, doi: [10.3847/1538-4357/ab68e6](https://doi.org/10.3847/1538-4357/ab68e6)
- Skelly, M. B., Unruh, Y. C., Collier Cameron, A., et al. 2008, *MNRAS*, 385, 708, doi: [10.1111/j.1365-2966.2008.12917.x](https://doi.org/10.1111/j.1365-2966.2008.12917.x)
- Skrutskie, M. F., Cutri, R. M., Stiening, R., et al. 2006, *AJ*, 131, 1163, doi: [10.1086/498708](https://doi.org/10.1086/498708)
- Stauffer, J., Collier Cameron, A., Jardine, M., et al. 2017, *AJ*, 153, 152, doi: [10.3847/1538-3881/aa5eb9](https://doi.org/10.3847/1538-3881/aa5eb9)
- Stauffer, J., Rebull, L., David, T. J., et al. 2018, *AJ*, 155, 63, doi: [10.3847/1538-3881/aaa19d](https://doi.org/10.3847/1538-3881/aaa19d)
- Stauffer, J., Rebull, L. M., Jardine, M., et al. 2021, *AJ*, 161, 60, doi: [10.3847/1538-3881/abc7c6](https://doi.org/10.3847/1538-3881/abc7c6)
- Stellingwerf, R. F. 1978, *ApJ*, 224, 953, doi: [10.1086/156444](https://doi.org/10.1086/156444)
- Tanimoto, Y., Yamashita, T., Ui, T., et al. 2020, *PASJ*, 72, 23, doi: [10.1093/pasj/psz145](https://doi.org/10.1093/pasj/psz145)
- Tofflemire, B. M., Rizzuto, A. C., Newton, E. R., et al. 2021, *AJ*, 161, 171, doi: [10.3847/1538-3881/abdf53](https://doi.org/10.3847/1538-3881/abdf53)
- Tokovinin, A., & Briceño, C. 2018, *AJ*, 156, 138, doi: [10.3847/1538-3881/aad906](https://doi.org/10.3847/1538-3881/aad906)
- Townsend, R. H. D. 2008, *MNRAS*, 389, 559, doi: [10.1111/j.1365-2966.2008.13462.x](https://doi.org/10.1111/j.1365-2966.2008.13462.x)
- Townsend, R. H. D., & Owocki, S. P. 2005, *MNRAS*, 357, 251, doi: [10.1111/j.1365-2966.2005.08642.x](https://doi.org/10.1111/j.1365-2966.2005.08642.x)
- Townsend, R. H. D., Owocki, S. P., & Groote, D. 2005, *ApJL*, 630, L81, doi: [10.1086/462413](https://doi.org/10.1086/462413)
- TRAPPIST-1 JWST Community Initiative, de Wit, J., Doyon, R., et al. 2024, *Nature Astronomy*, 8, 810, doi: [10.1038/s41550-024-02298-5](https://doi.org/10.1038/s41550-024-02298-5)
- Van Der Walt, S., Colbert, S. C., & Varoquaux, G. 2011, *Computing in Science & Engineering*, 13, 22
- van Eyken, J. C., Ciardi, D. R., von Braun, K., et al. 2012, *ApJ*, 755, 42, doi: [10.1088/0004-637X/755/1/42](https://doi.org/10.1088/0004-637X/755/1/42)
- Vial, J.-C., & Engvold, O. 2015, *Astrophysics and Space Science Library*, Vol. 415, Solar Prominences, doi: [10.1007/978-3-319-10416-4](https://doi.org/10.1007/978-3-319-10416-4)
- Vidotto, A. A., Jardine, M., Opher, M., Donati, J. F., & Gombosi, T. I. 2011, *MNRAS*, 412, 351, doi: [10.1111/j.1365-2966.2010.17908.x](https://doi.org/10.1111/j.1365-2966.2010.17908.x)
- Villarreal D'Angelo, C., Jardine, M., Johnstone, C. P., & See, V. 2019, *MNRAS*, 485, 1448, doi: [10.1093/mnras/stz477](https://doi.org/10.1093/mnras/stz477)
- Vines, J. I., & Jenkins, J. S. 2022, *MNRAS*, 513, 2719, doi: [10.1093/mnras/stac956](https://doi.org/10.1093/mnras/stac956)
- Virtanen, P., Gommers, R., Oliphant, T. E., et al. 2020, *Nature Methods*, 17, 261, doi: [10.1038/s41592-019-0686-2](https://doi.org/10.1038/s41592-019-0686-2)
- Virtanen, P., Gommers, R., Oliphant, T. E., et al. 2020, *Nature Methods*, 17, 261, doi: [10.1038/s41592-019-0686-2](https://doi.org/10.1038/s41592-019-0686-2)
- Vogt, S. S., Allen, S. L., Bigelow, B. C., et al. 1994, *SPIE Conference Series*, ed. D. L. Crawford & E. R. Craine, Vol. 2198
- Waugh, R. F. P., & Jardine, M. M. 2022, *MNRAS*, 514, 5465, doi: [10.1093/mnras/stac1698](https://doi.org/10.1093/mnras/stac1698)
- Winters, J. G., Henry, T. J., Jao, W.-C., et al. 2019, *AJ*, 157, 216, doi: [10.3847/1538-3881/ab05dc](https://doi.org/10.3847/1538-3881/ab05dc)
- Wood, M. L., Mann, A. W., Barber, M. G., et al. 2023, *AJ*, 165, 85, doi: [10.3847/1538-3881/aca8fc](https://doi.org/10.3847/1538-3881/aca8fc)
- York, D. G., Adelman, J., Anderson, John E., J., et al. 2000, *AJ*, 120, 1579, doi: [10.1086/301513](https://doi.org/10.1086/301513)
- Zhan, Z., Günther, M. N., Rappaport, S., et al. 2019, *ApJ*, 876, 127, doi: [10.3847/1538-4357/ab158c](https://doi.org/10.3847/1538-4357/ab158c)